Interplay between structural and thermoelectric properties in epitaxial $Sb_{2+x}Te_3$ alloys

S. Cecchi 1,, D. Dragoni 2, D. Kriegner 3,4, E. Tisbi 5, E. Zallo 1, F. Arciprete 1,5, V. Holy 3,6, M. Bernasconi 2, and R. Calarco 1*

1 Paul-Drude-Institut für Festkörperelektronik, Hausvogteiplatz 5-7, D-10117 Berlin, Germany.

2 Department of Materials Science, University of Milano-Bicocca, via R. Cozzi 55, 20125 Milano, Italy.

3 Department of Condensed Matter Physics, Faculty of Mathematics and Physics, Charles University, Ke Karlovu 5,12116 Praha, Czech Republic.

4 Max-Planck-Institute for Chemical Physics of Solids, Nöthnitzer Straße 40, 01187 Dresden, Germany

5 Dipartimento di Fisica, Università di Roma "Tor Vergata", Via della Ricerca Scientifica 1, I-00133 Rome, Italy.

6 CEITEC at Masaryk University, Kotlářská 2, 611 37 Brno, Czech Republic

*cecchi@pdi-berlin.de

Abstract

In recent years strain engineering has been proposed in chalcogenide superlattices to shape in particular the switching functionality for phase change memory applications. This is possible in Sb_2Te_3/GeTe heterostructures leveraging on the peculiar behavior of Sb_2Te_3, in between covalently bonded and weakly bonded materials. In the present study we characterize the structural and thermoelectric properties of epitaxial $Sb_{2+x}Te_3$ films, as they represent an intriguing option to expand the horizon of strain engineering in such superlattices. Samples with composition between Sb_2Te_3 and Sb_4Te_3 have been prepared by molecular beam epitaxy. A combination of X-ray diffraction and Raman spectroscopy, together with dedicated simulations, allows unveiling the structural characteristics of the alloys. A consistent evaluation of the structural disorder characterizing the material is drawn, as well as the presence of both Sb_2 and Sb_4 slabs is detected. A strong link exists among structural and thermoelectric properties, the latter having implications also in phase change superlattices. A further improvement of the thermoelectric performances may be achieved by accurately engineering the intrinsic disorder. The possibility to tune the strain in designed $Sb_{2+x}Te_3$/GeTe superlattices by controlling at the nanoscale the two dimensional character of the $Sb_{2+x}Te_3$ alloys is envisioned.

1. Introduction

Since the discovery of graphene, [1,2] two dimensional (2D) materials and related van der Waals (vdW) heterostructures have quickly become a vast playground for both basic and applied materials research, promising disrupting implications in flexible and transparent electronics and optoelectronics. [3] With respect to heterostructures prepared by exfoliation technique, [4] vdW epitaxy [5] guarantees better purity and scalability, both pivotal for device processing and implementation with the well established Si technology.

Antimony telluride (Sb_2Te_3) is a layered chalcogenide material formed by quintuple layers (QLs) bonded to each other by vdW forces. It has been studied for its topological insulating surface states [6] and used as building block in phase change memory (PCM) and thermoelectric (TE) superlattice (SL) structures. [7,8] A small interaction between substrate and epilayer has been shown for Sb_2Te_3 grown by molecular beam epitaxy (MBE) on both Si(111) [9] and graphene. [10] Very recently our group demonstrated an intriguing deviation from such a purely 2D material behavior. [11,12] Indeed, in epitaxial Sb_2Te_3/GeTe SLs a partial coupling develops between the constituting Sb_2Te_3 and GeTe layers. Strikingly, an unparalleled distribution of lattice parameters, which is tunable, develops in the heterostructures allowing also to realize strain engineering in such weakly coupled systems. This is of high interest, since strain engineering in chalcogenide SLs has been proposed for improved switching performance. [13,14]

Following these results, here we investigate $Sb_{2+x}Te_3$ alloys grown epitaxially by MBE on silicon substrate. Several antimony telluride lamellar phases exist in the homologous series $(Sb_2Te_3)_m(Sb_2)_n$, in which Sb_2 double layers (DLs) are inserted between Sb_2Te_3 QLs forming ordered stacking sequences (also named adaptive natural SLs). [15,16] While the composition related increase of the lattice parameter is well known and used in Ref. [14], the tuning of the 2D character of $Sb_{2+x}Te_3$ by finely controlling the excess of Sb in the material (i.e. to strengthen the coupling) may provide an additional tool to tailor the

functionality of chalcogenide SLs. Since for compositions between Sb_2Te_3 and Sb_4Te_3 the vdW gaps are progressively filled by the Sb DLs, the range of interest of our study is $Sb_{2+x}Te_3$ alloys with *x* between 0 and 2. In addition, considering PCM devices we remind that even small deviations of the GeSbTe (GST) composition affect markedly both electrical and thermal parameters. [17] Furthermore, as shown for the electrical transport properties of Sb_2Te_3/GeTe SLs, [18] the understanding and control of disorder which could be achieved by MBE may allow tailoring the thermoelectric properties of $Sb_{2+x}Te_3$ alloys.

In the following we focus exemplary on Sb_4Te_3. The crystal structure of Sb_4Te_3 is as well lamellar, however, two possible alternatives for the stacking order are proposed in literature. Poudeu and Kanatzidis [16] reported a "two to two" (2/2) stacking of two Sb DLs (Sb_4) alternated with two Sb_2Te_3 QLs belonging to the *R-3m* space group (Figure 1(a)). Soon afterwards Kifune et al. [19] suggested a "one to one" (1/1) stacking of a single Sb DL (Sb_2) followed by a QL (Figure 1(b)). The structure was not observed directly but was inferred by continuity in passing from Sb_2Te_3 to $Sb_{72}Te_{28}$ crystals all within the *R-3m* space group. Remarkably, the bonding nature of the Sb_4Te_3 1/1 and 2/2 packing sequences is different, since only in the latter case a vdW gap is generated between adjacent QLs. [16] Thus discerning and potentially controlling between the two structures is paramount to allow for strain engineering in such weakly coupled systems.

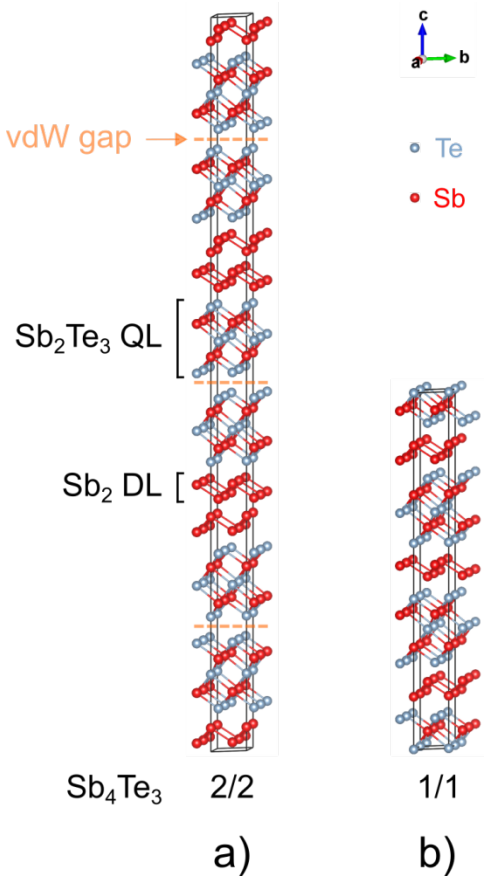

Figure 1: Sb_4Te_3 2/2 (a) and 1/1 (b) structures optimized by Density functional theory calculations (see Section 6).

2. Growth and X-Ray Diffraction

Details about the growth of epitaxial $Sb_{2+x}Te_3$ films are reported in Section 6. In Figure 2(a) the radial scans of the $Sb_{2+x}Te_3$ samples on normal Si(111) are shown (dotted lines). Starting from stoichiometric Sb_2Te_3, [9] the composition of $Sb_{2+x}Te_3$ was controlled by increasing the Sb/Te atomic flux ratio, providing the Sb excess by decreasing the Te flux while keeping fixed the Sb one. The sharp peaks at ~2, 4 and 6 $Å^{-1}$ correspond to the (111), (222), and (333) Bragg reflections of the Si substrate. Sb_2Te_3 radial scan

(brown curve) is characterized by a series of Bragg reflections along the symmetric rod (00.3*l*), reflecting its highly periodic layered structure. The separation between the peaks allows inferring the *c* lattice parameter (30.44 ± 0.11 Å), which is very close to previous reports. [20,21] In analogy to the $Bi_{2+x}Te_3$ system, [22] the excess of Sb produces remarkable structural changes in the material, as testified by the continuous evolution of the diffraction curves. Besides a reduction of the Q_z separation between 00.[3*(2+3*l*)] and 00.[3*(3+3*l*)] Sb_2Te_3 peaks (00.6-00.9, 00.15-00.18, 00.24-00.27 in Figure 2(a)), which is attributed to the overall increase of the *c* lattice parameter from Sb_2Te_3 to Sb_4Te_3 (and beyond), it is worth to emphasize the following points. i) Double peak features appear when low excess of Sb is provided (orange curve). Sb_2Te_3 00.12 and 00.21 peaks split, while shoulders at lower Q_z values are visible for 00.6 and 00.15 peaks. ii) The separation between these peaks follows the increase of Sb incorporated in the film, while their intensities weaken (yellow and magenta curves). iii) For the sample with the highest Sb content in the series (blue curve), only the peak at 4.67 $Å^{-1}$ is still visible and is narrower.

These double peak features are interpreted as a signature of $(Sb_2Te_3)_m(Sb_2)_n$ superstructures in the films. Indeed, as in the case of Sb_2Te_3, a series of satellite peaks along the symmetric rod is expected for a highly periodic stacking. The fact that in the present data only few of these peaks are visible indicates an irregular mixture of Sb_2Te_3 and Sb DLs in the $Sb_{2+x}Te_3$ films. Similarly to epitaxial $Bi_{2+x}Te_3$ films, [22] the repetition of Sb_2Te_3 and Sb_2 slabs during the growth is slightly inaccurate, resulting in a certain dispersion with respect to the ideally ordered stacking sequence. Still, the information about the average periodicity is preserved. Also, the weakening and broadening of the $(Sb_2Te_3)_m(Sb_2)_n$ superstructure features as a function of the excess of Sb indicate a gradual loss of order in the films. A relation between this observation and the decreasing growth rate in the series, measured by X-ray reflectivity (see Figure S1(a) and Table S1 in supplementary) can be excluded. In fact, very similar results have been obtained in different $Sb_{2+x}Te_3$ series where, starting from Sb_2Te_3, the Sb flux was increased to

provide the Sb excess while keeping the Te flux constant (shown below). The formation of non-continuous Sb_2 DLs as well as of thicker Sb_{2n} blocks can explain the loss of order. Moreover, additional shoulders appear in the samples with higher Sb content (magenta and blue curves), possibly revealing the formation of mixed $Sb_{2+x}Te_3$ phases. The presence of thicker Sb_{2n} blocks or even local Sb segregation cannot be excluded (see discussion in Section 3).

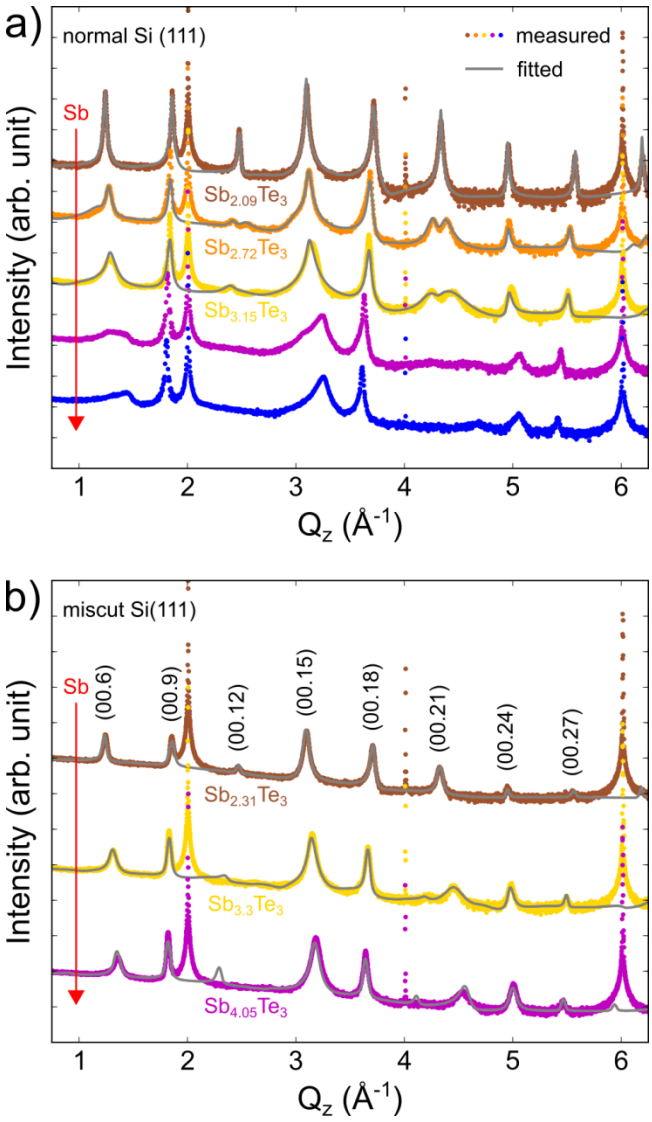

Figure 2: XRD radial scans of $Sb_{2+x}Te_3$ samples grown on (a) normal Si(111) and (b) miscut Si(111). Sb_2Te_3 curves are plotted in brown, while orange, yellow, magenta and blue curves correspond to Sb-rich samples with increasing excess of Sb. The curves are vertically shifted for clarity. The fitted curves (solid gray lines) are superposed to the measurements. The alloy compositions, as calculated from the fits, are also shown. The sharp peaks at ~2, 4 and 6 $Å^{-1}$ correspond to the (111), (222), and (333) Bragg reflections of the Si substrate. Sb_2Te_3 symmetric Bragg reflections are labeled in (b). The red arrows indicate the increase of Sb in the 2 series.

The XRD radial scans of our samples reveal a drastic change in the structure as a function of the excess of Sb. In particular, the highly periodic structure of Sb_2Te_3 is gradually lost. The appearance and change of characteristic features in the curves can be used to obtain information about the composition and structural quality of the alloys. Based on the statistical modeling developed to simulate $Bi_{2+x}Te_3$, [22] we implemented a fit routine for $Sb_{2+x}Te_3$ films. A marked difference with respect to bismuth telluride [23] is that in the present case Sb_{2n} blocks thicker than Sb_2 are likely to form. [16] For simplicity, in the present model we included only Sb_2 and Sb_4 slabs. In the model we assume that the crystal consists of a random sequence of QL-blocks separated by Sb_2 or Sb_4 slabs. The random numbers of QLs in different QL-blocks are statistically independent. The mean number N_{QL} of QLs in the QL-blocks, its root-mean square (rms) deviation *width* as wells as the probability p_{Sb4} of finding the Sb_4 slab were used as fitting parameters. Details about the modeling are reported in supplementary information.

The fitted curves are plotted in Figure 2(a) (solid gray lines) along with the experimental ones. The relevant parameters from the fits are collected in Tables 1 and S2. We first tested the consistency of the model with Sb_2Te_3 (brown curve in Figure 2(a)). Apart for small discrepancies in the intensity profile, all the features in the radial scan are nicely reproduced. Strikingly, our model allows to track even small

deviations from the stoichiometric Sb_2Te_3 composition (see Table 1). Then, we successfully performed the fit for the following two samples in the series (orange and yellow curves). In both cases, the matching between fit and experiment is rather good. The characteristic double features of $Sb_{2+x}Te_3$ alloys as well as their evolution as a function of the excess of Sb are well reproduced. Remarkably, we found that it was not possible to accurately fit the curves when only Sb_2 or Sb_4 slabs are stacked in the films (not shown here). Hence, our data show the coexistence of 1/1 and 2/2 Sb_4Te_3 sequences. At present, unfortunately, we were not able to fit the curves of the samples more rich in Sb. The higher structural disorder in these two samples, which is responsible for the disappearance of some of the peaks in XRD radial scans, prevents to obtain reliable fits. Moreover, the appearance of additional weak features in the curves may be possibly interpreted as a segregation of different phases, which cannot be reproduced by our model. Therefore, based on these results we can state that only for compositions in between Sb_2Te_3 and SbTe the stacking quality is still not heavily affected.

Table 1: Relevant parameters fitted for $Sb_{2+x}Te_3$ samples on normal and miscut Si. Those grown on miscut Si are marked with an asterisk. The N_{QL} parameter is the average number of Sb_2Te_3 blocks in between Sb_2(Sb_4) layers, while p_{Sb4} is the ratio between Sb_4 and Sb_2 slabs. Statistical errors obtained from the least squares optimization are below 5%.

sample	N_{QL} (# QLs)	p_{Sb4} (%)
$Sb_{2.09}Te_3$	24.7	21
$Sb_{2.72}Te_3$	3.5	25
$Sb_{3.15}Te_3$	2.0	18
$Sb_{2.31}Te_3$*	9.4	77
$Sb_{3.3}Te_3$*	1.7	22
$Sb_{4.05}Te_3$*	1.0	14

In a recent paper [24] we studied the epitaxy of GeSbTe alloys on passivated vicinal Si substrates, demonstrating the modulation between vdW and classical epitaxy induced by strain at the Si step edges. Interestingly, the use of miscut substrates also promotes the reduction of the compositional disorder typical of epitaxial GeSbTe. Based on this finding, we repeated the growth of $Sb_{2+x}Te_3$ films on low miscut Si substrates (see Experimental details) aiming to improve the structural quality. Three samples were prepared, intended to have compositions close to those plotted in brown (Sb_2Te_3), yellow (SbTe) and magenta (not fitted) in Figure 2(a). The XRD radial scans of these samples, along with the fitted curve for each one, are shown in Figure 2(b) (dotted and solid lines, respectively). The same colors as in Figure 2(a) have been used. The XRR measurements of the samples are shown in the supplementary (Figure S1(b)). The lower intensity of $Sb_{2+x}Te_3$ peaks with respect to those on normal Si, particularly evident for Sb_2Te_3, is ascribed to the different thickness between the samples (see Table S1). Remarkably, the features of $Sb_{2+x}Te_3$ in the radial scans are much sharper (see yellow and magenta curves in Figure 2(b)). For the latter, a distinct peak at 4.53 $Å^{-1}$ appears, while no additional shoulder is present. These improvements indicate a significant reduction of the structural disorder and allowed to fit the curves for all 3 samples (see solid gray lines in Figure 2(b)). In the results listed in Table S2 the sharper peaks of both yellow and magenta curves are reflected by an increased ratio of $N_{QL}/width$. Hence, this ratio can be effectively used to evaluate the structural disorder in $Sb_{2+x}Te_3$ films. For the last sample in the series (magenta) it equals the value of Sb_2Te_3, while the calculated composition is very close to Sb_4Te_3. Notably, p_{Sb4} is about 14%, confirming the formation of a mixed Sb_4Te_3 phase with both 1/1 and 2/2 stacking sequences.

Also, in both series p_{Sb4} consistently decreases when more Sb is incorporated. This trend seems to be counterintuitive; however it can be tentatively explained as follows. When an exiguous excess of Sb is provided (i.e. for $Sb_{2.72}Te_3$ 3.5 Sb_2Te_3 QLs are in average sandwiched between Sb_{2n} slabs), the layered nature of Sb_2Te_3 still dominates. Indeed, although it would in principle be possible to form only Sb_2 DLs,

the system preferentially stacks more consecutive Sb_2Te_3 blocks. As a consequence, in this sample about one quarter of the Sb layers is doubled (Sb_4). When more Sb is given, instead, this mechanism may be gradually hindered and less Sb_4 slabs are stacked.

3. Raman Spectroscopy

Complementary to XRD radial scans, Raman spectroscopy is a powerful tool which was demonstrated to be suitable to identify the different crystalline phases of GST [25] as well as to qualitatively access the vertical order in Sb_2Te_3/GeTe(GeSbTe) SLs. [18,26] Interestingly, in the case of $Sb_{2+x}Te_3$ this technique demonstrates excellent sensitivity to the structural changes induced by the excess of Sb, as shown in Figure 3(a) for the samples on normal Si. The Raman spectra of the $Sb_{2+x}Te_3$ films grown on miscut substrates are very similar to those on normal Si (see Figure S3(a)). Therefore, while XRD is more powerful to evaluate the structural disorder, Raman scattering allows in this case an estimation of the film composition. Not surprisingly, a red shift of the Sb_2Te_3 modes is clearly present along the series, related to the composition dependent increase of lattice parameters. In Figure S3(b) we plot the position of the $A_{1g}^{(1)}$ and $E_g^{(2)}$ modes for the series on miscut Si. More relevant, the $A_{1g}^{(1)}$ and $E_g^{(2)}$ modes are gradually suppressed, testifying the strong link of these vibrations with the layered structure of Sb_2Te_3, while the $A_{1g}^{(2)}$ one only broadens slightly. In particular the intense $A_{1g}^{(1)}$ mode, which completely vanishes in the last spectrum of the series, is the most affected. Also, new modes appear in the spectra (black arrows). (i) For all the samples with Sb excess ($x > 0.7$) a peak at ~98 cm^{-1} is visible. (ii) For $x \geq 1$ a broad peak centered at ~130 cm^{-1} gradually emerges. (iii) Finally, in the last 2 samples spectra ($x \geq 2$) fairly weak modes at about 147 cm^{-1}, 155 cm^{-1} and a shoulder at ~170 cm^{-1} rise.

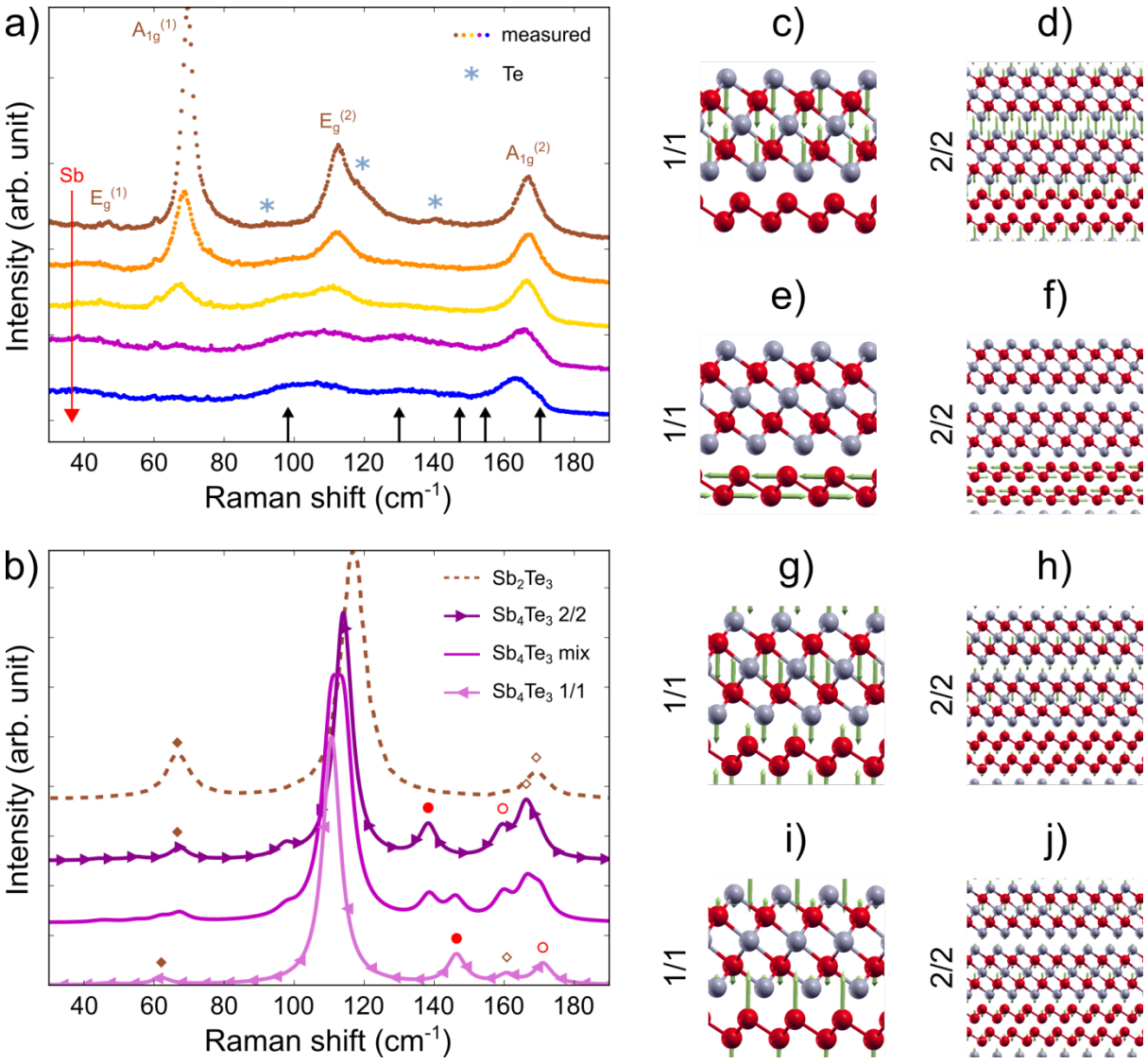

Figure 3: (a) Raman spectra of $Sb_{2+x}Te_3$ samples grown on normal Si(111). $Sb_{2.09}Te_3$ curve is plotted in brown (the modes of Sb_2Te_3 are also labeled), while orange ($Sb_{2.72}Te_3$), yellow ($Sb_{3.15}Te_3$), magenta and blue curves correspond to Sb-rich samples with increasing excess of Sb (see red arrow). The curves are vertically shifted for clarity. The black arrows indicate the features appearing in $Sb_{2+x}Te_3$ samples. The weak peaks at about 92, 119 and 140 cm^{-1} visible in the spectrum of Sb_2Te_3 (gray markers) are a signature of the presence of few Te segregated in the sample, as clarified in Figure S4. (b) Theoretical

Raman spectra for Sb_4Te_3 in the 1/1 and 2/2 structures, violet and purple curves with left and right triangle markers respectively, along with that of Sb_2Te_3 from the paper of Sosso et al., [27] dashed brown curve. The theoretical Sb_4Te_3 spectrum averaged over the 1/1 and 2/2 spectra is also shown (magenta curve). The spectra are normalized to the intensity of the peaks at about 110 cm^{-1} and vertically shifted for clarity. (c-j) Displacement patterns of relevant modes of Sb_4Te_3 for the 1/1 (c,e,g,i) and 2/2 (d,f,h,j) structures; Displacement patterns of the A_{1g} mode at (c) 62 cm^{-1} in the 1/1 structure and (d) 67 cm^{-1} in the 2/2 structure (highlighted in (b) with full brown squares); Displacement patterns of the E_g modes due to the Sb layers at (e) 146 cm^{-1} in the 1/1 structure and (f) 138 cm^{-1} in the 2/2 structure (highlighted in (b) with full red circles); Displacement patterns of the A_{1g} mode at (g) 160 cm^{-1} in the 1/1 structure and (h) 166 cm^{-1} in the 2/2 structure mostly localized on the Sb_2Te_3 layers (highlighted in (b) with empty brown squares); Displacement patterns of the A_{1g} mode at (i) 171 cm^{-1} in the 1/1 structure and (j) 159 cm^{-1} in the 2/2 structure mostly localized on the Sb bilayers (highlighted in (b) with empty red circles).

In order to uncover the structural evolution responsible for the changes measured in the Raman spectra, addressing in particular the origin of the additional modes, phonons at the *Γ* point and the corresponding Raman tensor are calculated within density functional perturbation theory (DFPT) for the two possible structures of Sb_4Te_3 (1/1 and 2/2). The resulting phonon frequencies are reported in Table S3. Details about the calculations are given in the experimental section and supplementary. We note that pure Sb also crystallizes in a trigonal structure (two atoms per unit cell) with an E_g mode at 115 cm^{-1} and an A_{1g} mode at 150 cm^{-1} visible in the experimental Raman spectrum [28]. Theoretical calculations for a single self-standing Sb bilayer [29] show that these two modes shift to higher frequency, namely at about 150 cm^{-1} (E_g) and 187 cm^{-1} (A_{1g}).

The theoretical Raman spectra of Sb_4Te_3 obtained for the 1/1 and 2/2 structures are plotted in Figure 3(b), along with that of Sb_2Te_3 from Ref. [27]. Our spectra for Sb_4Te_3 still display an intense peak around 110 cm^{-1} that is found for Sb_2Te_3 and that can be ascribed to the use of non-resonant conditions in our calculation (see supplementary). Therefore, in the comparison with experiments we disregard the intensity of this central peak and consider only the intensity ratio among the other peaks. A detailed description of the theoretical spectra of Sb_4Te_3 is reported in the supplementary. The main features which characterize the spectra are highlighted in Figure 3(b) with squares and circles. The corresponding displacement patterns are shown in Figure 3(c-j). The peaks marked with full and empty squares are A_{1g} modes involving mostly the motion of Sb_2Te_3 layers, which correspond to the two A_{1g} modes of Sb_2Te_3. These modes red shift when Sb DLs are introduced. Full and empty circles indicate, respectively, the E_g and the A_{1g} modes involving only the motion of the Sb bilayers. These correlate with the modes of bulk Sb and single self-standing Sb bilayer. A consistent red shift of both peaks, when increasing the number of Sb bilayers, is shown. Notably, a characteristic peak at about 97 cm^{-1} is present only in the spectrum of the Sb_4Te_3 2/2 structure. This is an E_g mode also localized on Sb_2Te_3, with the two Sb_2Te_3 layers in anti-phase. Therefore, this mode is a signature of adjacent Sb_2Te_3 QLs. In fact, no corresponding mode is found for Sb_4Te_3 (1/1) and Sb_2Te (see supplementary), both having a single Sb_2Te_3 QLs in between Sb slabs.

For what concerns the comparison with experiments the following comments can be raised. i) Moving from Sb_2Te_3 to Sb_4Te_3 in the 1/1 stacking all modes are red-shifted, in qualitative agreement with experiments. ii) The ratio between the peaks at about 160 cm^{-1} and that at about 60 cm^{-1} which is larger in Sb_4Te_3 than in Sb_2Te_3 is also reproduced by theory. iii) The agreement with the experimental spectra is overall better for the 2/2 structure, as highlighted in particular by the peak at about 97 cm^{-1} (~98 cm^{-1} in the experiments), which is not present in the theoretical spectrum of the 1/1 structure. However, this does not exclude the presence of both structures in the films. In fact, the broad feature at ~130 cm^{-1} and

the peak at 147 cm^{-1} in the experimental spectra could be assigned to a mixture of the mode at 146 cm^{-1} of the 1/1 structure and that at 138 cm^{-1} of the 2/2 structure, the latter eventually shifted to lower frequency possibly because of the coexistence of other structures with thicker Sb_{2n} blocks. iv) The mixing of the modes at 160 cm^{-1} (1/1) and 166 cm^{-1} (2/2) contributes in major part to the red shift and broadening of the $A_{1g}^{(2)}$ mode of Sb_2Te_3 in the experiments. The additional features at about 155 cm^{-1} and 170 cm^{-1}, which are only present in the samples with composition of Sb_4Te_3 and above, could be explained as signatures of the 2/2 (red shifted as that at 138 cm^{-1}) and 1/1 structures, respectively.

Therefore, this interpretation is in agreement with our XRD simulations. Assuming that disorder in the stacking arises in the experimental samples leading to the coexistence of the 1/1 and 2/2 structures, a more compelling qualitative comparison between theory and experiments could be made by averaging the theoretical spectra of the two structures as shown in Figure 3(b) (magenta curve).

4. Electrical Characterization

Table 2: Transport and thermoelectric properties of $Sb_{2+x}Te_3$ samples at 300 K. The hole concentration *p*, the carrier mobility μ, the Seebeck coefficient *S*, the electrical conductivity σ and the power factor *PF* are reported.

Sample	p (10^{20} cm^{-3})	μ ($cm^2V^{-1}s^{-1}$)	S (μVK^{-1})	σ (10^3 Scm^{-1})	PF ($mWm^{-1}K^{-2}$)
$Sb_{2.31}Te_3$*	1.05	107.44	118	1.81	2.52
$Sb_{3.3}Te_3$*	6.98	14.17	41	1.58	0.35
$Sb_{4.05}Te_3$*	10.80	10.26	30	1.78	0.16

Table 2 summarizes the room temperature (RT) transport and TE properties of the samples grown on miscut Si(111). In accordance with the works of Takagaki [30] and Kuznetsov [31], the samples have p-type conduction and the hole concentration *p* is linearly proportional to the excess of Sb in the alloys (see Figure S5). The carrier mobility μ and the thermopower *S* as a function of the hole concentration are shown in Figure 4. The relationship between μ and *p* is well reproduced by a $\mu \propto p^{-1}$ curve (dashed black line). This is as well in agreement with the data reported by Kuznetsov, [31] interpreted by the authors as a result of scattering from impurities with concentration equal to the hole concentration. We recently found that the intrinsic structural disorder in Sb_2Te_3/GeTe SLs limits the carrier mobility while introducing additional carriers in the material. [18] Native Sb_2Te_3/$Ge_xSb_2Te_{3+x}$ SLs, in which the mitigation of intermixing results in a reduced density of stacking faults, have indeed improved carrier mobility. Accordingly here, as explained in the previous sections, the structural quality typical of Sb_2Te_3 is gradually affected by the increase of Sb in the material. Therefore, our results again emphasize the direct link between structural quality and electrical properties in layered chalcogenides. Since the metallic character of the compounds increases following the excess of Sb, the Seebeck coefficient decreases. The dependence between *S* and *p* can be approximated by a $S \propto p^{-2/3}$ curve (dashed gray line). This nicely follows the behavior described by simple models of electron transport for metals or degenerate semiconductors, [32] assuming that the carriers effective mass is independent of the film composition in the investigated range. Comparing our results with those of Poudeu and Kanatzidis, [16] the RT thermopower values of Sb_1Te_1 samples are close to each other, while interestingly that of Sb_4Te_3 is about a factor 3 higher in our case. We interpret this finding as a further indication of the improved structural quality, namely less additional carriers, [18] achieved for epitaxial $Sb_{2+x}Te_3$ on miscut Si substrates. Clearly, the TE properties of alloys richer in Sb are more affected by their structural properties. In the case of $Sb_{2.31}Te_3$, the measured thermopower is slightly lower compared to values reported for Sb_2Te_3 thin films in the literature, [33–35] reflecting the small excess of Sb in the film.

The electrical conductivity σ and the power factor $S^2\sigma$ as a function of the Sb excess are shown in Figure S6. A rather small variation of the electrical conductivity between the studied samples is reported (< 15%), as expected considering the p^{-1} relationship between mobility and hole concentration. This is again in line with the data of Kuznetsov and coworkers, [31] but differs from the results of Poudeu and Kanatzidis [16] where σ was reported to continuously decrease from Sb_8Te_9 to Sb_2Te. The power factor dependence on the Sb content is mostly dominated by that of the thermopower. It ranges between 160 $\mu Wm^{-1}K^{-2}$ for $Sb_{4.05}Te_3$ and 2.52 $mWm^{-1}K^{-2}$ for $Sb_{2.31}Te_3$. Despite the slight Sb excess, this last value is about 5 and 11 times larger than those reported for Sb_2Te_3 grown by MBE [33] and atomic layer deposition [35] respectively, while it approaches that of Sb_2Te_3 fabricated by nanoalloying method. [34,36] Similar power factor values are also reached for co-evaporated Sb_2Te_3 films. [37–39]

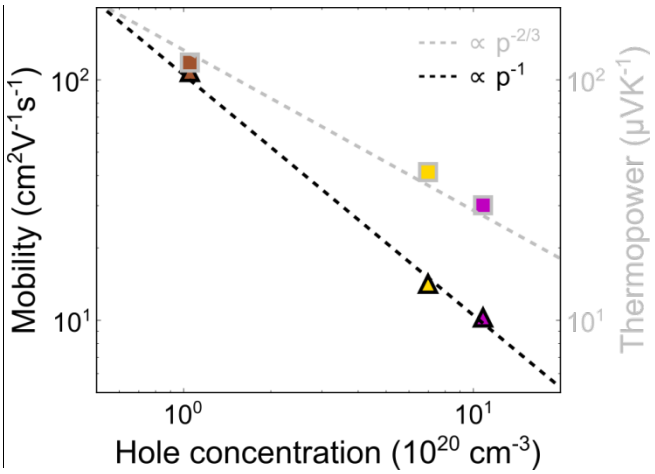

Figure 4: RT carrier mobility (triangles with black border) and thermopower (squares with gray borders) as a function of the hole concentration of the $Sb_{2+x}Te_3$ films grown on miscut Si. The black and gray dashed lines are a $k_\mu p^{-1}$ curve with $k_\mu = 1.05\times10^2$ $cm^{-1}V^{-1}s^{-1}$ and a $k_S p^{-3/2}$ curve with $k_S = 1.33\times10^2$ $cm^{-2}\mu VK^{-1}$, respectively. Both curves are meant to be guide to the eyes.

5. Conclusion and Outlook

In conclusion, we fabricated epitaxial $Sb_{2+x}Te_3$ alloys on Si(111) substrates by means of MBE. A combination of XRD and Raman spectroscopy measurements allows to efficiently access the composition and structural properties of the material. The simulations we developed for both sets of data give an insight into the intrinsic disorder in our samples with respect to $(Sb_2Te_3)_m(Sb_2)_n$ adaptive natural SLs. Based on the present study, a rapid assessment of the composition of $Sb_{2+x}Te_3$ alloys can be drawn by Raman spectroscopy.

In-plane electrical and TE characterization of the films with compositions close to Sb_2Te_3, SbTe and Sb_4Te_3 at RT is reported. Noteworthy, these data demonstrate the improved TE properties of epitaxial Sb_4Te_3, which are strongly linked to the structural quality achieved in the material. Since some disorder is still present in the samples grown on miscut Si, a further increase of the thermopower may be possibly achieved in highly ordered Sb_4Te_3 superstructures. More promising is the case of $Sb_{2+x}Te_3$ alloys with low excess of Sb ($x < 1$). The scenario is different, yet it closely relates to the structural properties of the material. In fact, while we record thermopower values in line with previous reports, the higher electrical conductivity boosts the power factor in the $mWm^{-1}K^{-2}$ range. Clearly, the present achievement is driven by the relatively high carrier mobility despite the carrier concentration is above 10^{20} cm^{-3}, once more paradigmatic of the interplay between structural and electrical properties in these materials. Moreover, we expect to further enhance the thermopower by accurately reducing the excess of Sb in the film while ensuring to follow the $\mu \propto p^{-1}$ curve in Figure 4 in order to keep constant the electrical conductivity.

Concerning PCM applications, the situation is more complex since the memory devices are typically operated in the cross-plane direction. Therefore, considering only the in-plane electrical properties it is

not trivial to predict the effect on the switching performance of SL devices. With respect to the alloy composition, the electrical conductivity does not change in our case. This means that the electronic contribution to the in-plane thermal conductivity is also unchanged (Wiedemann-Franz law), while we do not expect additional phonon scattering since the Sb slabs have sub nm size. For the same alloy composition, instead, a reduction of the structural disorder is expected to improve the in-plane carrier mobility. [18] Moreover, the material anisotropy becomes larger, possibly affecting the switching. In fact, the heat generated during the device operation would preferentially flow laterally rather than vertically, meaning that a higher power is required to complete the switching. At the same time, however, the more efficient lateral heat flow may favor a faster switching. Also, epitaxial $Sb_{2+x}Te_3$ films are much smoother compared to Sb_2Te_3, as shown in the Supplementary (Figure S1). This as well should play a role in improving the SL structural quality.

As mentioned in the introduction, $Sb_{2+x}Te_3$ alloys were proposed to realize strain engineered phase change SLs, leveraging on the larger lattice parameter. [14] To this end, the present results demonstrate that the control of the structure of $(Sb_2Te_3)_m(Sb_2)_n$ natural SLs at the nanoscale is fundamental. In fact, the formation of incomplete Sb DLs as well as of thicker Sb blocks would hinder the realization of fully coupled heterostructures, reducing the effective strain exerted on the GeTe layers. [12] Ultimately, MBE offers a unique possibility for the growth of $Sb_{2+x}Te_3$ alloys which could potentially be exploited to control at the nanoscale both the stacking sequence and the ordering. The same applies also to other V_2VI_3 chalcogenides. It paves the way for the demonstration of a novel concept in material science, where the strain in the heterostructure can be readily tuned by engineering the number of vdW gaps per unit thickness, tailoring the V_2VI_3 properties in between those of 2D and 3D materials.

6. Experimental Section

Sample preparation: $Sb_{2+x}Te_3$ films were fabricated by MBE on on Si(111)-(√3 × √3)R30°-Sb passivated surfaces. Both normal Si(111) and miscut Si(111) (1.25° along HKL) were used. The latter are also high-resistivity Si (> 5000 Ωcm), allowing to avoid the contribution of the substrate while measuring lateral electrical transport properties. The substrate cleaning method and the preparation of the Si(111)- (√3 × √3)R30°-Sb surface were described by Wang et al.. [40] Starting from stoichiometric Sb_2Te_3, [9] the composition of $Sb_{2+x}Te_3$ was controlled by increasing the Sb/Te atomic flux ratio, providing the Sb excess either decreasing the Te flux while keeping fixed the Sb one (series on normal Si(111)) or vice versa (series on miscut Si(111)). All other growth parameters were unchanged.

X-ray diffraction: The diffractometer used for the XRD and XRR characterization is a PANalytical X' Pert PRO MRD system with a Ge(220) hybrid monochromator, employing a CuKα_1 (λ = 1.540598 Å) X-ray radiation. The data analysis was carried out using Xrayutilities. [41]

X-ray diffraction simulation: Details about the modeling are reported in supplementary information. The main parameters in the model are the average number of Sb_2Te_3 blocks in between Sb_2(Sb_4) layers (N_{QL}), the ratio between Sb_4 and Sb_2 layers (p_{Sb4}) and the rms deviation of the number of QLs in the QL-blocks (*width*). The alloy composition can be directly calculated from the first two parameters, while the third one is an indication of the dispersion with respect to the average stacking.

Raman spectroscopy: The Raman spectra were acquired in backscattering z(y,xy)-z geometry, the sample was excited with the 632.8 nm line of a He–Ne laser, and the scattered light was analyzed using a spectrometer equipped with an liquid N_2-cooled charge-coupled device (CCD) detector. The emission was focused by a microscope objective with 0.9 numerical aperture and the same objective was used for the collection of the signal. The spatial resolution achieved is 0.7 cm^{-1} and a notch filter suppressed the stray light.

Density functional theory calculations: We have optimized the geometry of the Sb_4Te_3 (1/1) and (2/2) structures by means of Density Functional Theory (DFT) calculations using the Quantum-Espresso suite of programs, [42] the Perdew-Burke-Ernzerhof exchange and correlation functional [43] and the van der Waals correction due to Grimme (D2). [44] The optimized lattice parameters are reported in Table S3 for the two structures. The 2/2 structure is lower in energy by 5 meV per atom. The theoretical Raman spectra at 300 K are computed within density functional perturbation theory [45] for non-resonant conditions in backscattering geometry along the *c* axis and for non-polarized light. A Lorenzian broadening of 3 cm^{-1} is assigned to all peaks. The Bose factor is computed at 300 K.

Thermoelectric characterization: Lateral electrical transport properties of $Sb_{2+x}Te_3$ samples were studied by Hall measurements at 300 K. In order to avoid a contribution of the substrate, the 3 samples have been grown on high-resistivity Si(111) (>5000 Ωcm). A four-contact van der Pauw configuration was realized by wire bonding the samples to the chip carriers using In droplets and Au wires. The measurements were performed applying currents and magnetic fields of 0.5 mA and 0.5 T, respectively. The measurements relative errors are < 10^{-4} and < 10^{-2} for the sheet resistance and the Hall resistance, respectively. The measurements of the Seebeck coefficient were performed on the same 3 samples. A Peltier cooling element was used to apply the temperature gradient (~3°C in 7 steps). Ag conductive paste in between the Peltier element and the sample is needed to improve the thermal contact conductance. The voltage difference was measured in a two-contact configuration.

Acknowledgments

S.C. designed the experiments with contributions from R.C. and F.A.. S.C. and F. A. performed the growths on normal Si, while S.C. and E. T. those on miscut Si. XRD characterization and analysis was mostly carried out by S.C. with the support of F.A.. XRD simulations were carried out by S.C. and D.K. with the support of V.H.. The code was implemented by D.K. in analogy with that developed by V.H. for previous studies. E.Z. performed the Raman spectroscopy measurements. The DFT and DFPT calculations were carried out by D.D.. The analysis of Raman spectroscopy data and comparison with calculations was carried out by S.C., D.D. and M.B.. All the authors discussed the results. The paper was written by S.C., with the help and contributions from all co-authors. The project was conceptualized by R.C..

This work was partially supported by EU within the FP7 project PASTRY (GA 317746) and partly by the Leibniz Gemeinschaft within the Leibniz Competition on a project entitled: “Epitaxial phase change superlattices designed for investigation of non-thermal switching”. D.K. and V.H. acknowledge the support of the project NanoCent financed by European Regional Development Fund (ERDF, project No. CZ.02.1.01/0.0/0.0/15_003/0000485).

The authors declare no competing interest.

We thank S. Behnke and C. Stemmler for technical support at the molecular beam epitaxy system, M.Ramsteiner for support with Raman systems, A. Riedel for support with the Hall measurement setup and A. Papadogianni for support with the Seebeck measurements. M. Ramsteiner, Y. Takagaki are acknowledged for helpful discussions and X.Y. for careful reading of the manuscript.

References

[1] K. S. Novoselov, A. K. Geim, S. V Morozov, D. Jiang, Y. Zhang, S. V Dubonos, I. V Grigorieva, A. A. Firsov, *Science (80-.).* **2004**, *306*, 666.

[2] C. Berger, Z. Song, T. Li, X. Li, A. Y. Ogbazghi, R. Feng, Z. Dai, N. Alexei, M. E. H. Conrad, P. N. First, W. a. De Heer, *J. Phys. Chem. B* **2004**, *108*, 19912.

[3] G. Fiori, F. Bonaccorso, G. Iannaccone, T. Palacios, D. Neumaier, A. Seabaugh, S. K. Banerjee, L. Colombo, *Nat. Nanotechnol.* **2014**, *9*, 768.

[4] K. S. Novoselov, D. Jiang, F. Schedin, T. J. Booth, V. V Khotkevich, S. V Morozov, A. K. Geim, *Proc. Natl. Acad. Sci. U. S. A.* **2005**, *102*, 10451.

[5] A. Koma, *Thin Solid Films* **1992**, *216*, 72.

[6] Y. Takagaki, A. Giussani, K. Perumal, R. Calarco, K.-J. Friedland, *Phys. Rev. B* **2012**, *86*, 125137.

[7] R. Simpson, P. Fons, A. Kolobov, T. Fukaya, M. Krbal, T. Yagi, J. Tominaga, *Nat. Nanotechnol.* **2011**, *6*, 501.

[8] R. Venkatasubramanian, E. Siivola, T. Colpitts, B. O'Quinn, *Nature* **2001**, *413*, 597.

[9] J. E. Boschker, J. Momand, V. Bragaglia, R. Wang, K. Perumal, A. Giussani, B. J. Kooi, H. Riechert, R. Calarco, *Nano Lett.* **2014**, *14*, 3534.

[10] J. E. Boschker, L. A. Galves, T. Flissikowski, J. M. J. Lopes, H. Riechert, R. Calarco, *Sci. Rep.* **2015**, *5*, 18079.

[11] S. Cecchi, R. N. Wang, E. Zallo, R. Calarco, *Nanosci. Nanotechnol. Lett.* **2017**, *9*, 1114.

[12] R. Wang, F. R. L. Lange, S. Cecchi, M. Hanke, M. Wuttig, R. Calarco, *Adv. Funct. Mater.* **2018**, *28*, 1.

[13] J. Kalikka, X. Zhou, E. Dilcher, S. Wall, J. Li, R. E. Simpson, *Nat. Commun.* **2016**, *7*, 11983.

[14] X. Zhou, J. Kalikka, X. Ji, L. Wu, Z. Song, R. E. Simpson, *Adv. Mater.* **2016**, *28*, 3007.

[15] L. E. Shelimova, O. G. Karpinskii, V. I. Kosyakov, V. A. Shestakov, V. S. Zemskov, F. A. Kuznetsov, *J. Struct. Chem.* **2000**, *41*, 81.

[16] P. F. P. Poudeu, M. G. Kanatzidis, *Chem. Commun.* **2005**, 2672.

[17] M. Boniardi, A. Redaelli, I. Tortorelli, S. Lavizzari, A. Pirovano, F. Pellizzer, E. Varesi, D. Erbetta, C. Bresolin, A. Modelli, R. Bez, *2012 4th IEEE Int. Mem. Work. IMW 2012* **2012**, 31.

[18] S. Cecchi, E. Zallo, J. Momand, R. Wang, B. J. Kooi, M. A. Verheijen, R. Calarco, *APL Mater.* **2017**, *5*, 026107.

[19] K. Kifune, Y. Kubota, T. Matsunaga, N. Yamada, *Acta Crystallogr. B.* **2005**, *61*, 492.

[20] T. L. Anderson, H. B. Krause, *Acta Crystallogr. Sect. B Struct. Crystallogr. Cryst. Chem.* **1974**, *30*, 1307.

[21] H. Zhang, Y. Cheng, M. Tang, X. Chen, G. Ji, *Comput. Mater. Sci.* **2015**, *96*, 342.

[22] H. Steiner, V. Volobuev, O. Caha, G. Bauer, G. Springholz, V. Holý, *J. Appl. Crystallogr.* **2014**, *47*, 1889.

[23] K. Yamana, K. Kihara, T. Matsumoto, *Acta Crystallogr. Sect. B* **1979**, *0505*, 147.

[24] E. Zallo, S. Cecchi, J. E. Boschker, A. M. Mio, F. Arciprete, S. Privitera, R. Calarco, *Sci. Rep.* **2017**, *7*, 1466.

[25] V. Bragaglia, K. Holldack, J. E. Boschker, F. Arciprete, E. Zallo, T. Flissikowski, R. Calarco, *Sci. Rep.* **2016**, *6*, 28560.

[26] E. Zallo, R. Wang, V. Bragaglia, R. Calarco, *Appl. Phys. Lett.* **2016**, *108*, 221904.

[27] G. C. Sosso, S. Caravati, M. Bernasconi, *J. Phys. Condens. Matter* **2009**, *21*, 095410.

[28] X. Wang, K. Kunc, I. Loa, U. Schwarz, K. Syassen, *Phys. Rev. B - Condens. Matter Mater. Phys.* **2006**, *74*, 1.

[29] D. Campi, M. Bernasconi, G. Benedek, *Phys. Rev. B - Condens. Matter Mater. Phys.* **2012**, *86*, 075446.

[30] Y. Takagaki, A. Giussani, J. Tominaga, U. Jahn, R. Calarco, *J. Phys. Condens. Matter* **2013**, *25*, 345801.

[31] P. I. Kuznetsov, B. S. Shchamkhalova, V. O. Yapaskurt, V. D. Shcherbakov, V. A. Luzanov, G. G. Yakushcheva, V. A. Jitov, V. E. Sizov, *J. Cryst. Growth* **2017**, *471*, 1.

[32] M. Cutler, J. F. Leavy, R. L. Fitzpatrick, *Phys. Rev.* **1964**, *133*.

[33] Y. Kim, A. DiVenere, G. K. L. Wong, J. B. Ketterson, S. Cho, J. R. Meyer, *J. Appl. Phys.* **2002**, *91*, 715.

[34] M. Winkler, X. Liu, J. D. König, S. Buller, U. Schürmann, L. Kienle, W. Bensch, H. Böttner, *J. Mater. Chem.* **2012**, *22*, 11323.

[35] S. Zastrow, J. Gooth, T. Boehnert, S. Heiderich, W. Toellner, S. Heimann, S. Schulz, K. Nielsch, *Semicond. Sci. Technol.* **2013**, *28*, 035010.

[36] N. Peranio, M. Winkler, Z. Aabdin, J. König, H. Böttner, O. Eibl, *Phys. Status Solidi* **2012**, *209*, 289.

[37] L. M. Goncalves, P. Alpuim, A. G. Rolo, J. H. Correia, *Thin Solid Films* **2011**, *519*, 4152.

[38] J.-H. Kim, J. Choi, J. Bae, M. Kim, T. Oh, *Mater. Trans.* **2013**, *54*, 618.

[39] H. Shen, S. Lee, J. gu Kang, T. Y. Eom, H. Lee, S. Han, *Appl. Surf. Sci.* **2018**, *429*, 115.

[40] R. Wang, J. E. Boschker, E. Bruyer, D. Di Sante, S. Picozzi, K. Perumal, A. Giussani, H. Riechert, R. Calarco, *J. Phys. Chem. C* **2014**, *118*, 29724.

[41] D. Kriegner, E. Wintersberger, J. Stangl, *J. Appl. Crystallogr.* **2013**, *46*, 1162.

[42] P. Giannozzi, S. Baroni, N. Bonini, M. Calandra, R. Car, C. Cavazzoni, D. Ceresoli, G. L. Chiarotti, M. Cococcioni, I. Dabo, A. Dal Corso, S. de Gironcoli, S. Fabris, G. Fratesi, R. Gebauer, U. Gerstmann, C. Gougoussis, A. Kokalj, M. Lazzeri, L. Martin-Samos, N. Marzari, F. Mauri, R. Mazzarello, S. Paolini, A. Pasquarello, L. Paulatto, C. Sbraccia, S. Scandolo, G. Sclauzero, A. P. Seitsonen, A. Smogunov, P. Umari, R. M. Wentzcovitch, *J. Phys. Condens. Matter* **2009**, *21*, 395502.

[43] J. P. Perdew, K. Burke, M. Ernzerhof, *Phys. Rev. Lett.* **1996**, *77*, 3865.

[44] S. Grimme, *J. Comput. Chem.* **2006**, *27*, 1787.

[45] S. Baroni, S. De Gironcoli, A. Dal Corso, P. Giannozzi, *Rev. Mod. Phys.* **2001**, *73*, 515.